Crossover among structural motifs in Pd–Au nanoalloys

B. Zhu, H. Guesmi, J. Creuze, Bernard Legrand, C. Mottet

PCCP

PAPER

Cite this: *Phys. Chem. Chem. Phys.*, 2015, **17**, 28129

Crossover among structural motifs in Pd–Au nanoalloys

Beien Zhu,†[ab] Hazar Guesmi,[b] Jérôme Creuze,[c] Bernard Legrand[d] and Christine Mottet*[e]

Received 26th January 2015,
Accepted 26th February 2015

DOI: 10.1039/c5cp00491h

www.rsc.org/pccp

The crossovers among the most abundant structural motifs (icosahedra, decahedra and truncated octahedra) of Pd–Au nanoalloys have been determined theoretically in a size range between 2 and 7 nm and for three compositions equivalent to Pd_3Au, PdAu and $PdAu_3$. The chemical ordering and segregation optimisation are performed *via* Monte Carlo simulations using semi-empirical tight-binding potentials fitted to *ab initio* calculations. The chemical configurations are then quenched *via* molecular dynamic simulations in order to compare their energy and characterize the equilibrium structures as a function of the cluster size. For the smaller sizes (of around 300 atoms and fewer) the structures are also optimized at the electronic level within *ab initio* calculations in order to validate the semi-empirical potential. The predictions of the crossover sizes for the nanoalloys cannot be simply extrapolated from the crossover of the pure nanoparticles but imply stress release phenomena related to the size misfit between the two metals. Indeed, alloying extends the range of stability of the icosahedron beyond that of the pure systems and the energy differences between decahedra and truncated octahedra become asymptotic, around the sizes of 5–6 nm. Nevertheless, such equilibrium results should be modulated regarding kinetic considerations or possible gas adsorption under experimental conditions.

1 Introduction

Since the discovery of the catalytic activity of gold nanoparticles supported on oxide surfaces,[1] Au-based alloys nanoparticles have become attractive in order to elucidate the origin of the reactivity of gold.[2] Pd–Au catalysts have been shown to be very efficient for various reactions[3–6] and in particular in CO oxidation.[7,8] The understanding of the reactive mechanism requires a control of the composition, structure and chemical ordering at the surface. Moreover, many experimental studies have shown that gas adsorption-induced surface segregation occurs at the Pd–Au surface[4–7,9] during catalytic reactions, which is in good agreement with theoretical predictions on surfaces[10–12] or small clusters.[13,14] Moreover, in the case of CO oxidation, it has been shown experimentally that a higher performance of the Pd–Au catalysts was reached under high CO pressure[8] thanks to the Pd surface segregation and the formation of Pd-dimers or chains which are necessary for the O_2 dissociation, whereas the remaining gold atoms enable CO adsorption and desorption.

Within the hypothesis of vacuum conditions, another question which has not been addressed up to now concerns the equilibrium structure and morphology of Pd–Au nanoparticles in a large range of size. This question has been answered for quite small Pd–Au nanoalloys (fewer than 100 atoms)[15,16] with various symmetries or for pure clusters in a large range of size,[17,18] determining the crossover among structural motifs with high symmetry. Other studies focused on a thermodynamical study of the equilibrium ordering of Pd–Au nanoalloys,[19,20] but much less on the characterization of the most stable structure and morphology as a function of cluster size, up to many nanometers in size to be compared to most of the experimental results. Following a first study on the CoPt nanoalloy system[21] where the TOh motifs were theoretically stabilized from 2 to 3 nm and above, we will study the crossover sizes among the most probable motifs for three compositions of the Pd–Au alloys: Pd_3Au, PdAu and $PdAu_3$. The results differ from the Co–Pt system and cannot be simply deduced from the equilibrium shape of the pure nanoparticles.

This paper is composed of five sections: starting with the present Introduction, we then present the Model and simulation methods, and a comparison between the SMA and DFT calculations for the smallest cluster sizes (fewer than 300 atoms). In the

[a] *CNRS-LRS, UMR 7197, Laboratoire de Réactivité de Surface, Université Pierre et Marie Curie, 4 place Jussieu, 75252 Paris, France*
[b] *ICGM/MACS-UMR5253, 8 rue de l'Ecole Normale, F-34296 Montpellier, France*
[c] *Paris Sud University, ICMMO/SP2M, UMR8182, 15 rue Georges Clmenceau, Orsay, F-91405, France*
[d] *SRMP-DMN, CEA Saclay, Gif-sur-Yvette, F-91191, France*
[e] *Aix Marseille Université, CNRS, CINAM UMR7325, Campus de Luminy, F-13288 Marseille, France. E-mail: mottet@cinam.univ-mrs.fr*
† Present address: Division of Interfacial Water and Key Laboratory of Interfacial Physics and Technology, Shanghai Institute of Applied Physics, Chinese Academy of Sciences, Shanghai, 201800 China.

third section, the Crossovers among the different motifs are illustrated. The fourth section displays isotherms for each motif in order to detail the atomic structure and chemical configuration and to analyse the crossover in terms of stress release. The Conclusions are resumed in the fifth section.

2 Model and simulation methods

We performed Monte Carlo and quenched molecular dynamics simulations using a tight binding semi-empirical potential within the second moment approximation of the density of states (SMA potential). This many-body potential has been fitted to *ab initio* calculations within the density functional theory (DFT). Some of the smaller sizes of clusters (fewer than 300 atoms) have been also calculated within the DFT starting from the configuration optimized by Monte Carlo and quenched molecular dynamics simulations using the SMA potential.

The SMA potential is a semi-empirical method, fitted to bulk properties, which is able to give qualitative results on the crossover sizes among different structural motifs in a large size range. The method cannot predict the exact crossover size with precision but gives a reliable estimation of the sequence and the range of sizes of the transitions. For the smaller sizes where the potential is less reliable, we used DFT calculations to check the SMA results.

2.1 DFT calculations

The DFT calculations are performed using the Vienna Ab initio Simulation Package (VASP) code and the projector augmented wave (PAW)[22,23] interaction potential between the electrons and the ions. The exchange and correlation functional are either the local-density approximation (LDA)[24] or the generalized gradient approximation (GGA).[25] The Brillouin zone integration is performed with the Monkhorst–Pack scheme with *k*-point mesh comprising 12 subdivisions along each reciprocal lattice vector. The convergence criterion for the electronic self-consistent cycle is fixed to 10^{-6} eV and the geometry optimization is performed within the conjugate-gradient algorithm until the convergence of the force is less than 10^{-2} eV Å^{-1}.

The values of the lattice parameters, the cohesive energies and the surface energies have been calculated for the two metals (Table 1). The lattice parameters and the surface energies are better reproduced using the LDA functional as compared to the experimental values so that we chose the LDA results to fit the SMA potential.[26] For the alloys, the permutation of one impurity in each metal and the dissolution enthalpies have been calculated in the two diluted limits[26] (Table 2). The dissymmetry between the two limits is in good agreement with the one observed within DFT-GGA calculations[27] and experimental values.[28] The calculated dissolution enthalpy are lower than the experimental one but they correspond to the disordered alloy whereas it is not clear if the experimental mixing enthalpy at 300 K corresponds to the ordered or disordered state because the experimental critical temperatures are not well defined in that system.[28]

Table 1 Lattice parameter, cohesive energy and surface energies of Pd and Au. The experimental values are taken from Kittel, *Introduction to solid state physics*, Wiley, New York, 8th edn, 2005, for lattice parameters, p. 20, and cohesive energy, p. 50, and De Boer *et al.*, *Cohesion in metals*, North-Holland, Amsterdam, 1988, p. 662, for surface energies

Metal	a (Å)	E_{coh} (eV per at.)	$\gamma^{(100)}$ (eV per at.)	$\gamma^{(111)}$ (eV per at.)
Pd (LDA)	3.85	−4.98	0.95	0.74
Au (LDA)	4.08	−4.24	0.65	0.50
Pd (GGA)	3.96	−3.71	0.76	0.59
Au (GGA)	4.18	−3.04	0.48	0.31
Pd (exp.)	3.89	−3.94	0.94	—
Au (exp.)	4.08	−3.81	0.78	—

Table 2 DFT-LDA permutation and dissolution enthalpies from Creuze *et al.*[26] compared to the experimental values in the two diluted limits of the mixing enthalpies at 300 K[28]

(eV per at.)	Pd(Au)	Au(Pd)
ΔH^{perm}	0.63	−1.01
ΔH^{dissol}	−0.11	−0.26
ΔH^{dissol} (exp.)	−0.20	−0.38

For the calculations performed on small clusters (Section 2.4), the Gamma point was used in the Brillouin-zone integration of all the considered clusters and a cubic cell with the side of 3 nm was chosen to provide enough spacing between the metal clusters in the neighboring repeated cells.

2.2 SMA potential

This potential derives from the tight binding model in the so-called second moment approximation (SMA)[29] where the attractive term reproduces the second moment of the density of state of the metal inducing a square root dependence with the neighboring atoms whereas the repulsive term is a pairwise Born Mayer potential. The potential energy at site i for an atom of type a is then written as follows:

$$E_i^a = -\sqrt{\sum_{j,r_{ij}<r_{ab}^c} \xi_{ab}^2 e^{-2q_{ab}\left(\frac{r_{ij}}{r_{ab}^0}-1\right)}} + \sum_{j,r_{ij}<r_{ab}^c} A_{ab} e^{-p_{ab}\left(\frac{r_{ij}}{r_{ab}^0}-1\right)} \quad (1)$$

where r_{ij} is the distance between the atom at site i and their neighbors at site j, r_{ab}^c is the cut-off distance and r_{ab}^0 is the first neighbor distance depending on the nature of the atoms, and p_{ab}, q_{ab}, A_{ab}, ξ_{ab} are four parameters (listed in Table 4), which are fitted to the DFT values (Table 1) of the cohesive energies, lattice parameters and elastic constants for the pure metals, and to the mixing energies in the diluted limits (Table 2). It is well known that the SMA potential underestimates the surface energies but not homogeneously. As a consequence, other parameterizations[15] lead to the underestimation of the difference of the surface energies of the two elements, whereas such a quantity is a driving force for surface segregation,[30] and particularly in

Table 3 SMA potential values of the surface energies of Pd and Au

Metal	$\gamma^{(100)}$ (eV per at.)	$\gamma^{(111)}$ (eV per at.)
Pd	0.65	0.51
Au	0.35	0.26

Table 4 Parameters of the Pd–Au SMA potential

a–b	p_{ab}	q_{ab}	A_{ab}	ξ_{ab}
Pd–Pd	11.75280	2.87486	0.14352	1.88570
Au–Au	10.71890	4.09805	0.22043	1.97573
Pd–Au	11.23585	3.48645	0.21410	2.08060

Table 5 Mixing enthalpies (in meV per at.) calculated with the Pd–Au SMA potential in the ordered phases (DO_{22} for Pd_3Au and $PdAu_3$, and A_2B_2 for the PdAu) and compared with the experimental ones[28]

	Pd_3Au	PdAu	$PdAu_3$
SMA	−45	−79	−66
Exp.	−50	−80	−75

this system.[26] Therefore in this study, the parameters of the pure elements have been fitted to reproduce the difference of the surface energies of the two elements as obtained by DFT calculations (*cf.* Tables 1 and 3). Finally, a cut-off after the fourth neighbor distance r^c_{ab} is introduced which depends on the metal for the homoatomic interactions and we take the larger one for the heteroatomic interactions: $r^c_{ab} = \max\{r^c_{aa}, r^c_{bb}\}$.

This potential leads to mixing enthalpies of the ordered phases which are in good agreement with the experimental values at room temperature (see Table 5). However, as mentioned previously, we are not sure whether these experimental mixing enthalpies at 300 K (ref. 28) correspond to the ordered phases in the experiments. A more detailed comparison between LDA, GGA and experimental results will be provided in an upcoming study.[31]

2.3 Numerical simulations

We proceed with two types of simulations to get the comparison between the different motifs in Pd–Au nanoalloys. First, using Monte Carlo simulations in a semi-grand canonical (S-GCMC) or canonical (CMC) ensemble, we optimize the chemical configuration of different motifs of high symmetry for the clusters: icosahedron (Ih), decahedron (Dh) or truncated octahedron (TOh). Starting from these structures with well defined symmetries,[17] we propose random atomic exchanges (within CMC) or permutations (within S-GCMC) and small random atomic displacements around each atom. In the S-GCMC the difference between the two chemical potential remains constant and the concentration evolves toward the equilibrium concentration, whereas in the CMC, the concentration remains constant. In both simulations, the pressure, the temperature and the total number of atoms are constant. The Metropolis sampling insures that a Boltzmann distribution of the chemical configurations at equilibrium and finite temperature is reached. At low temperature and concerning the relaxation of the atomic positions, the Metropolis algorithm is less efficient so we use quenched molecular dynamics to get the ground state at 0 K.

2.4 Comparison between the DFT and SMA results for the smaller sizes (fewer than 300 atoms)

Because the SMA potential has been fitted to bulk properties, it is not so reliable as to determine the energy of very small clusters within a molecular state. So in that subsection we would like to compare the energies of these small systems (fewer than 300 atoms) calculated within the SMA potential, with the energies obtained using DFT calculations. Starting from the equilibrium configurations as obtained *via* the CMC optimization with the SMA potential, the positions of the ions have been further optimized within the DFT-LDA and -GGA calculations. The results are shown in the Fig. 1 for the pure clusters and in the Fig. 2 for the nanoalloys of compositions 1/4 and 3/4 in gold. Instead of plotting the average energy per atom, we plotted the energetic quantity usually considered in the comparison of pure nanoclusters of different sizes[17] and which can be extended to nanoalloys in the following way:[32]

$$\Delta = (E_N - N_{Au}E^{Au}_{coh} - N_{Pd}E^{Pd}_{coh})/N^{2/3}$$

where E_N is the total energy of the system of N atoms from which we substract the cohesive energy E^a_{coh} of the N_a atoms of

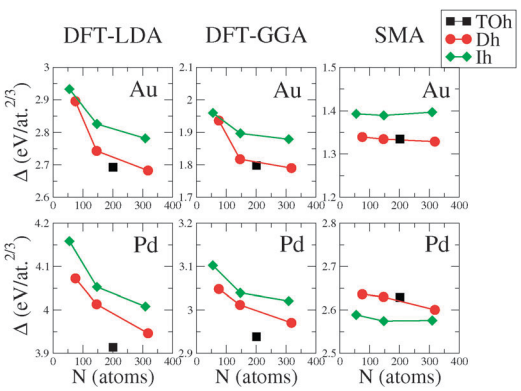

Fig. 1 Energy at 0 K of the different motifs: Ih, Dh and TOh monometallic Pd and Au clusters calculated by DFT-LDA and -GGA, and with the SMA potential.

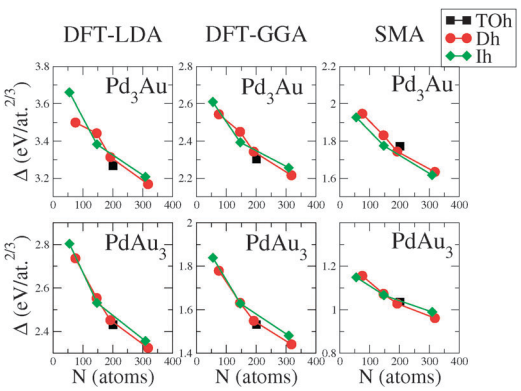

Fig. 2 The same as in Fig. 1 for the nanoalloys of composition Pd_3Au and $PdAu_3$.

the metal a in order to determine an excess energy with respect to the bulk of the pure elements, divided by $N^{2/3}$ which roughly scales as the number of surface atoms. Such quantity is relevant in what concerns the pure systems where it emphasises the difference in surface energy and excess core energy of the different structures, but it is not the case for the nanoalloys where the mixing energy equal to the excess energy between the alloy with respect to the pure elements in their bulk is strongly attenuated when divided by $N^{2/3}$. However, in this section we only pay attention to the comparison between the DFT and the SMA results. Concerning the crossover size we will use another criterion detailed in the next section.

We first notice in Fig. 1 and 2 that the LDA and GGA are very similar except in the absolute value of Δ which is less important. Then we notice that the SMA potential gives good qualitative ordering stability between the different structures for gold systems (Fig. 1) and rich-gold nanoalloys ($PdAu_3$ in Fig. 2). For Pd clusters, the SMA potential stabilizes the Ih at small sizes, whereas DFT stabilizes the TOh structure. In the SMA potential, the TOh and the Dh are degenerated. However, looking at larger sizes, the SMA potential finally stabilizes the Dh structure (Fig. 3). For the Pd-rich nanoalloys, the difference between the two models are less important since the DFT calculations also favor the Ih of 55 and 147 atoms, as the SMA potential. The TOh_{201} Pd_3Au nanoalloy in DFT is also more stable than in the SMA potential.

As a conclusion, without the aim of determining some crossover size between the different motifs for such small clusters (less than 300 atoms) and also because the simple symmetries considered here are not representative of the most stable structures at these sizes,[15,16] we simply conclude that our SMA potenial is in good agreement with the DFT calculations for pure gold clusters and alloyed systems but fails to reproduce the DFT calculations for pure Pd ones and to a less extent for Pd_3Au ones. This gives quite a good level of confidence for the results presented in the next section with the SMA potential concerning the crossover size among different motifs in nanoalloys, whatever the failing of the potential as compared to the DFT for the pure Pd small clusters.

3 Crossovers among different motifs

Before considering the bimetallic systems, we first show in Fig. 3 the crossovers of the pure systems with high symmetry structures (Ih, Dh and TOh) as obtained in previous studies.[17,18] The diameter of the nanoparticles is approximated by the following formula:

$$D = \frac{1}{2}\left(\frac{N}{4}\right)^{1/3}$$

where we consider that the number of atoms N is roughly proportional to the volume V of the nanoparticle of radius R so that $V = (4/3)\pi R^3 \sim 4R^3$ leads to $R \sim \left(\frac{N}{4}\right)^{1/3}$. Then we take a coefficient equal to the average interatomic distance of 0.25 nm between R and $\left(\frac{N}{4}\right)^{1/3}$ and $D = 2R$. This is a rough approximation of the nanoparticle diameter but we checked it was not so bad by measuring the exact diameter of some of the nanoparticles in this size range.

We notice in Fig. 3 that for Pd clusters, the Ih is stable up to size of 3 nm (about 1000 atoms), then Dh are stable between 3 and about 9 nm, after which the TOh should have become stable but we did not further extend our calculations. This is completely different for the gold clusters since the Ih is never stable and Dh and TOh structures are almost degenerated.

The crossovers of the Pd–Au nanoalloys are illustrated in Fig. 4 where for better clarity we plotted the difference in energies between the Ih or Dh structure and the TOh structure. The crossover in nanoalloys appears at much larger sizes as compared to pure clusters. Indeed, when adding gold in palladium clusters, the Ih structure remains stable in a larger range of sizes, up to 6 nm (6000 atoms) as compared to less than 3 nm (1000 atoms) for pure palladium clusters. At equiconcentration of Au and Pd, the Ih is still stable up to sizes of 3 nm (1000 atoms)

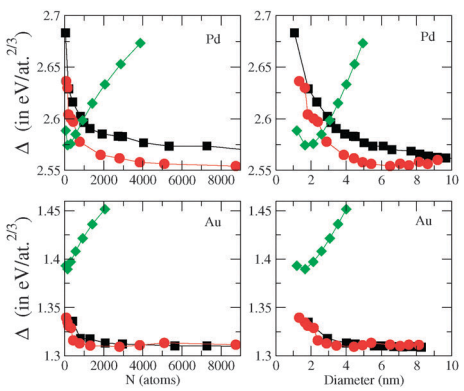

Fig. 3 Energies of the different high symmetry motifs (Ih, Dh and TOh) for pure Pd and Au clusters as a function of cluster size represented by the number of atoms N (left column) or the diameter D (right column) of the nanoparticle.

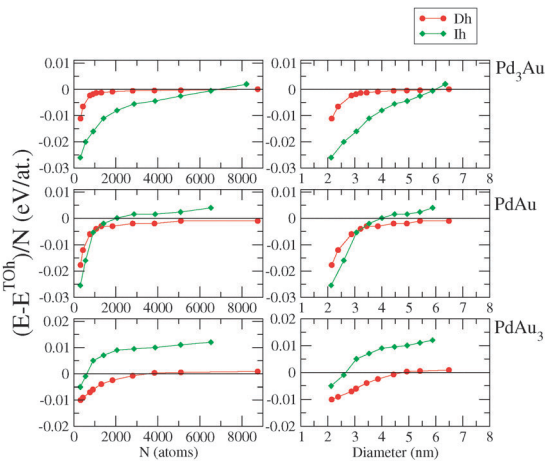

Fig. 4 Relative energy as refered to the TOh structure (zero energy) for the Ih and Dh motifs of Pd_3Au, PdAu and $PdAu_3$ compositions as a function of cluster size represented by the number of atoms N (left column) or the diameter D (right column) of the nanoparticle.

and for rich-gold clusters, the Dh is stabilized for sizes smaller than 4 nm (2000 atoms).

The Ih structure is stabilized in nanoalloys in a larger range of size than in the pure systems of equivalent size. The Dh structure in nanoalloys converges toward the TOh structure at size about 3 nm (1000 atoms) for the composition Pd_3Au and PdAu. In the $PdAu_3$ systems, the convergence is delayed but the difference in energy remains very small (3 meV per at. at 4 nm *i.e.* for 2000 atoms). We can notice that in that case the TOh structure becomes favorable above sizes of 5 nm (4000 atoms).

These results cannot be deduced from a weighted average of the pure systems. For example, in the pure Au systems, the Dh has almost the same energy as the TOh whereas in the pure Pd systems Dh presents a lower energy than the TOh in a large range of size. However, the Dh nanoalloys are more favourable in the Au-rich systems. Concerning the Ih nanoalloys, the range of stability of this structure is much larger as compared to the pure systems: however the tendency for going from pure Pd to pure Au systems is respected. This means that the Pd-rich nanoalloys present the largest range of stability, then the PdAu nanoalloys, and then the Au-rich ones.

We have no explanation for interpreting the results concerning the relative stability of the Dh as compared to the TOh, but we will give some insights to illustrate the results of the Ih nanoalloys in the next section. For that purpose, we will focus on the evolution of the stability of the Ih structure between pure metals and nanoalloys, especially looking at the chemical configurations, the surface segregation and core ordering using the segregation isotherms.

4 Segregation isotherms and internal stress

The chemical ordering and surface segregation are analyzed using S-GCMC in order to give a complete description of the chemical arrangement inside the nanoalloys $Pd_{1-c}Au_c$ as a function of the Au concentration $c = c_{Au}$ for each motif: TOh_{8678}, Dh_{8755} and Ih_{6525}. We chose large sizes to give an average representation of the typical chemical arrangement for each motif.

The global concentration in gold (c_{Au}) and the surface concentration for each type of surface site (vertex, edges, (100) and (111) facets) and the core concentration are plotted in Fig. 5, which gives an overview of the segregation isotherms at 100 K. First of all we can notice that the TOh and the Dh display almost identical isotherms, whatever their difference in atomic structure and morphology, except for the (100) facets where we notice a slight difference which also concerns a very small range of composition: less than 20% of gold.

An overall gold surface segregation is obtained in agreement with the experimental results under vacuum conditions[33,34] and segregation at the edge is in good agreement with DFT calculations.[33]

It is worth noticing, secondly, that there is an important surface segregation sequence starting at the vertices, then on the edges, and then at the (100) and (111) facets. This leads to an almost perfect core–shell structure as can be seen in

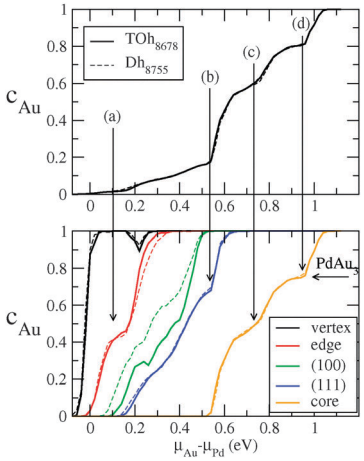

Fig. 5 Isotherms at 100 K for the TOh_{8678} and Dh_{8755} of $Pd_{1-c}Au_c$ nanoalloys giving the global concentration (c_{Au}) (top) and the concentration on each type of sites: vertex, edge, (100), (111) facets, and the core (bottom) as a function of the difference in chemical potential: $\mu_{Au} - \mu_{Pd}$; peculiar compositions (a), (b), (c) and (d) are illustrated in Fig. 6.

Fig. 6(b), where only the (111) facets are not pure in gold. They are chemically ordered for a facet composition of about 66% of gold which corresponds to the $(\sqrt{3} \times \sqrt{3})R30$ (111) superstructure in infinite surfaces. The ordering tendency leads to form mixed bonds where Pd atoms are surrounded by Au atoms inside the (111) facets. The surface segregation roughly respects the hierarchy of the broken bonds at the surface but there can be some interactions between the segregation in the different sites and some chemical ordering in each type of site. For example we get a specific vertex and edge Au segregation where

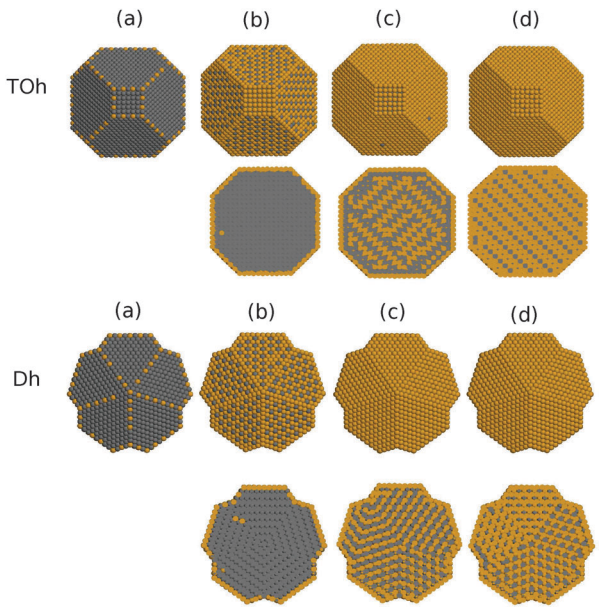

Fig. 6 Snapshots of the chemical configurations at 100 K of the TOh_{8678} and Dh_{8755} nanoalloys of $Pd_{1-c}Au_c$ corresponding to the peculiar compositions quoted in Fig. 5. Au atoms are represented in yellow and Pd atoms in grey. The second and fourth lines correspond to cutting views.

the ordering tendency of the alloy leads to alternate Au and Pd atoms along the edges and the vertices, corresponding to pure Au vertices and an almost equiatomic concentration on the edges (Fig. 5 and 6(a)).

Moreover, we notice that the isotherms display some irregularities which means that surface segregation and chemical ordering take place at given compositions at the surface and in the core. The illustrations of Fig. 6 correspond to the different shoulders on the isotherms representing peculiar ordering on the edges (a), on the (111) facets as detailed before (b), but also inside the core for core compositions of around 50% (c) and 75% of gold (d). In the case of the TOh structure, the core gets order following the A_2B_2 ordered phase at concentration around c_{core} = 0.50 (but with defects) and following the DO_{22} around c_{core} = 0.75, which are the phases of the bulk phase diagram obtained with the SMA potential[31] and in good agreement with theoretical studies of ordering properties of Au–Pd alloys and nanoalloys.[19] We will not characterize here the ordering of the core with possible antiphase boundaries, which would need deeper analysis. In the case of the Dh structure, the core also gets order, but with a multitwinned structure composed of five slightly distorted tetrahedral units which share two by two one (111) faces as twinned planes. We can notice locally ordered phases of the $L1_0$ type (c) or the $L1_2$ type (d) as compared to the A_2B_2 and DO_{22} ones in the TOh symmetry. We do not investigate deeper into the understanding of that chemical arrangement even if it raises interesting questions, but this will be attempted in further studies.

The same isotherms at 100 K have been determined for the Ih_{6525} nanoalloys and are shown in Fig. 7. The overall shape of the global isotherm (global composition as a function of the difference in chemical potential) is not so different from the one of the Dh or TOh structures and the main characteristic is the almost core–shell structure with the gold segregation at the surface which corresponds to the weak slope at the beginning of the curve. However the surface of the Ih is different because there are only facets of the (111) type. There is the same shoulder on the edges as for the Dh or TOh structures, corresponding to

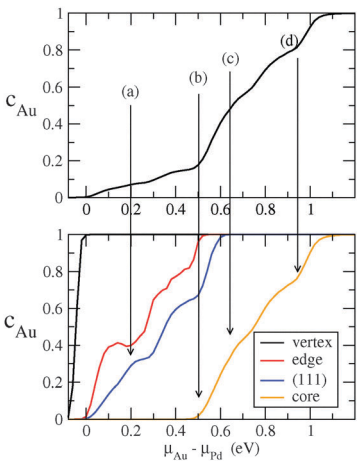

Fig. 7 Isotherms at 100 K of the Ih_{6525} nanoalloys of $Pd_{1-c}Au_c$ as in Fig. 5. The second and fourth lines correspond to cutting views.

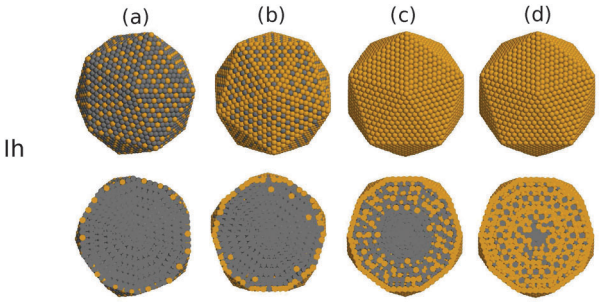

Fig. 8 Snapshots of the chemical configurations at 100 K of the Ih_{6525} nanoalloys of $Pd_{1-c}Au_c$ corresponding to the peculiar compositions quoted in Fig. 7. The second line corresponds to cutting views.

the alternation of Pd and Au atoms along the edges. More surprisingly, the edge concentration is then no more monotonic. It is probably related to their coupling with the concentration of these (111)-type facets. These facets clearly present two shoulders looking like "plateaus" roughly corresponding to the $(\sqrt{3} \times \sqrt{3})$R30 (111) surface structure previously mentioned at 33% and 66% of gold. The corresponding structures are illustrated in Fig. 8(a) and (b) where the minority atoms are surrounded by the majority ones.

Then, there is a change in the slope of the isotherm corresponding to the core enrichment with gold, at the vicinity of the surface, as we can see in Fig. 8(b). The gold atoms are located near the surface, but not on the subsurface, which is in agreement with theoretical studies[35,36] where the smaller atoms prefer to segregate at the subsurface. In the Pd–Au system, the smaller atoms are the Pd atoms so that we get the segregation of Pd at the subsurface. By increasing the gold concentration, the gold atoms are located exclusively in the neighborhood of the surface and not in the center of the Ih (see Fig. 8(c)), the center remaining pure in Pd even for high concentrations of gold (see Fig. 8(d)).

We have to recall here that the Ih structure is strongly compressed in its core, especially at its center, until it is relaxed by the introduction of a vacancy,[37] or by an impurity with a smaller atomic radius.[38] Such stress relaxation also induced the equilibrium properties of so-called magic polyicosahedral core-shell clusters.[39] More recently, a study related to the role of mechanical stress in the chemical ordering of Au–Pd nanoalloys has shown the influence of the stress on the chemical ordering in Ih.[20]

We plotted in Fig. 9 the local pressure on each concentric layer defined according to the variation of the energy as a function of a variation of the atomic volume:[40]

$$p_i = -\frac{dE_i}{d\ln V_i} = -\frac{1}{3}\sum_j \frac{dE_i}{dr_{ij}} r_{ij}$$

where E_i is the energy at site i and r_{ij} the interatomic distance between the atom at site i and its neighbors at site j. This local pressure is converted in pressure units (GPa per at.) upon dividing by an appropriate atomic volume. We can notice in Fig. 9 that the pure Pd and Au Ih have the highest compression at the center of the cluster, whereas upon introduction of 45%

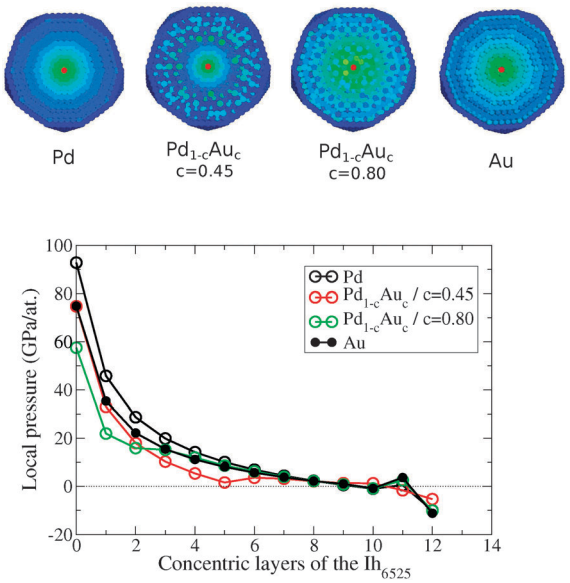

Fig. 9 Local pressure at O K of the Ih_{6525} nanoalloys of $Pd_{1-c}Au_c$ average on each atomic layer (in GPa per at.) as a function of the concentric layers of the Ih starting from its central atom (0) up to the surface (12); the snapshots with cutting views give an illustration of the atomic pressure map of the nanoalloys with a color code going progressively from the deep blue color corresponding to the atoms in tension to the red color corresponding to the atoms in strong compression.

of gold into the Pd cluster, the stress is considerably released from the center up to the sixth layer which amounts to around half of the radius of the nanoparticle. This corresponds to the cluster represented in the Fig. 8(c). Then, going on to replace Pd atoms by gold atoms to reach a composition of 80% of gold (Fig. 8(d)), the stress is still more released in the very center of the Ih. The nanoalloy with 80% of gold, where Pd segregates to the center, has released the stress in the center as compared to pure gold Ih. So that finally the Ih nanoalloys tend to locally release the stress as compared to the pure systems.

This is also what we can conclude if we consider the total stress over each particle. Indeed, when we know how the stress is distributed inside the Ih between the tensile zone at the surface and the compressive zone in the core, we can ask how the total stress varies, knowing it should be globally equal to zero since there is no external pressure applied on the nanoparticle. In fact the residual total stress in the pure clusters is hundred times larger than the one in the nanoalloys: −4.64 GPa for the Pd Ih, −0.62 GPa for the pure Au Ih and only 0.04 and 0.02 for the 45% and 80% nanoalloys.

Following the argument that we can stabilize the nanoalloys *via* release of the mechanical stress energy, this gives an explanation for extending the range of stability of the Ih nanoalloy structures as compared to their pure counterparts.

5 Conclusions

Using a semi-empirical SMA interatomic potential fitted to *ab initio* calculations, we determined for the first time the crossover sizes among different structural motifs in a large range of sizes: between 2 and 7 nm. Although the Ih structure is never stabilized in pure gold clusters and at very small sizes for pure Pd clusters (less than 3 nm or one hundred atoms), the Ih structure is stable in a large range of size in Pd_3Au and PdAu nanoalloys (up to 6 nm for Pd_3Au and 3 nm for PdAu). This can be well explained regarding the core stress in the Ih structure which can be released by replacing large atoms by smaller ones in nanoalloys. The crossover sizes between Dh and TOh structures are not well defined and we rather obtain a convergence between the energies of these structures for Pd_3Au and PdAu nanoalloys. For the $PdAu_3$ systems, the crossover is reached after 5 nm. This is a first attempt to characterize the structure and morphology of Pd–Au nanoalloys in a large range of sizes to be compared to the experiments; however, such results may change in the presence of gas or by considering possible kinetic effects under experimental conditions.

Acknowledgements

We acknowledge support from the French Research National Agency under the Project ANR-11-JS07-0007, the EU COST Action MP0903, the the French HCP resources: CCRT/CINES/IDRIS under the allocations 2012[x2012086395] and 2013-096829. The first author also thanks for the development fund for Shanghai talents (Y439011011).

References

1 M. Haruta, *Gold. Bull.*, 2004, **37**, 27–36.
2 H. Zhang, T. Watanabe, M. Okumura, M. Haruta and N. Toshima, *Nat. Mater.*, 2012, **11**, 49–52.
3 M. S. Cheng, D. Kumar, C. W. Yi and D. W. Goodman, *Science*, 2005, **310**, 291–293.
4 L. Piccolo, A. Piednoir and J.-C. Bertolini, *Surf. Sci.*, 2005, **592**, 169–181.
5 A. Hugon, L. Delannoy, J. Krafft and C. Louis, *J. Phys. Chem. C*, 2010, **114**, 10823–10835.
6 N. E. Kolli, L. Delannoy and C. Louis, *J. Catal.*, 2013, **297**, 79–92.
7 F. Gao, Y. Wang and D. W. Goodman, *J. Phys. Chem. C*, 2009, **113**, 14993–15000.
8 F. Gao, Y. Wang and D. W. Goodman, *J. Phys. Chem. C*, 2010, **114**, 4036–4043.
9 L. Delannoy, S. Giorgio, J. G. Mattei, C. R. Henry, N. E. Kolli, C. Mthivier and C. Louis, *ChemCatChem*, 2013, **5**, 2707–2716.
10 V. Soto-Verdugo and H. Metiu, *Surf. Sci.*, 2007, **601**, 5332–5339.
11 H. Guesmi, C. Louis and L. Delannoy, *Chem. Phys. Lett.*, 2011, **503**, 97–100.
12 A. Dhouib and H. Guesmi, *Chem. Phys. Lett.*, 2012, **521**, 98–103.
13 P. S. West, R. L. Johnston, G. Barcaro and A. Fortunelli, *J. Phys. Chem. C*, 2010, **114**, 19678–19686.

14 B. Zhu, G. Thrimurthulu, L. Delannoy, C. Louis, C. Mottet, J. Creuze, B. Legrand and H. Guesmi, *J. Catal.*, 2013, **308**, 272–281.
15 F. Pittaway, L. O. Paz-Borbon, R. L. Johnston, H. Arslan, R. Ferrando, C. Mottet, G. Barcaro and A. Fortunelli, *J. Phys. Chem. C*, 2009, **113**, 9141–9152.
16 A. Bruma, R. Ismail, L. O. Paz-Borbon, H. Arslan, G. Barcaro, A. Fortunelli, Z. Y. Li and R. L. Johnston, *Nanoscale*, 2013, **5**, 646–652.
17 F. Baletto, R. Ferrando, A. Fortunelli, F. Montalenti and C. Mottet, *J. Chem. Phys.*, 2002, **116**, 3856–3863.
18 C. Mottet, J. Goniakowski, F. Baletto, R. Ferrando and G. Tréglia, *Phase Transitions*, 2004, **77**, 101–113.
19 I. Atanasov and M. Hou, *Surf. Sci.*, 2009, **603**, 2639–2651.
20 B. Zhu and M. Hou, *Eur. Phys. J. D*, 2012, **66**, 63–71.
21 P. Andreazza, C. Mottet, C. Andreazza-Vignolle, J. Penuelas, H. C. N. Tolentino, M. De Santis, R. Felici and N. Bouet, *Phys. Rev. B*, 2010, **82**, 155453.
22 P. E. Blöchl, *Phys. Rev. B*, 1994, **50**, 17953–17979.
23 G. Kresse and D. Joubert, *Phys. Rev. B*, 1999, **59**, 1758–1775.
24 G. Kresse and J. Hafner, *Phys. Rev. B*, 1993, **47**, 558–561.
25 J. P. Perdew and Y. Wang, *Phys. Rev. B*, 1992, **45**, 13244–13249.
26 J. Creuze, H. Guesmi, C. Mottet, B. Zhu and B. Legrand, *Surf. Sci.*, 2015, submitted.
27 M. H. F. Sluiter, C. Colinet and A. Pasturel, *Phys. Rev. B*, 2006, **73**, 174204.
28 R. Hultgren, P. D. Desai, D. T. Hawkins, M. Gleiser and K. K. Kelley, *American Society for Metals*, Metal Park, Ohio, 1973.
29 V. Rosato, M. Guillopé and B. Legrand, *Phil. Mag. A*, 1989, **59**, 321.
30 J. Creuze, I. Braems, F. Berthier, C. Mottet, G. Tréglia and B. Legrand, *Phys. Rev. B*, 2008, **78**, 075413.
31 J. Creuze, B. Zhu, H. Guesmi, C. Mottet and B. Legrand, 2015, in preparation.
32 A. Rapallo, G. Rossi, R. Ferrando, A. Fortunelli, B. C. Curley, L. D. Lloyd, G. M. Tarbuck and R. L. Johnston, *J. Chem. Phys.*, 2005, **122**, 194308.
33 H. L. Abbott, A. Aumer, Y. Lei, C. Asokan, R. J. Meyer, M. Sterrer, S. Shaikhutdinov and H.-J. Freund, *J. Phys. Chem. C*, 2010, **114**, 17099–17104.
34 A. R. Haire, J. Gustafson, A. G. Trant, T. E. Jones, T. C. Noakes, P. Bailey and C. J. Baddeley, *Surf. Sci.*, 2011, **605**, 214–219.
35 C. Langlois, Z. L. Li, J. Yuan, D. Alloyeau, J. Nelayah, D. Bochicchio, R. Ferrando and C. Ricolleau, *Nanoscale*, 2012, **4**, 3381–3388.
36 D. Bochicchio and R. Ferrando, *Phys. Rev. B*, 2013, **87**, 165435.
37 C. Mottet, G. Tréglia and B. Legrand, *Surf. Sci.*, 1997, **383**, L719–L727.
38 C. Mottet, G. Rossi, F. Baletto and R. Ferrando, *Phys. Rev. Lett.*, 2005, **95**, 035501.
39 G. Rossi, A. Rapallo, C. Mottet, A. Fortunelli, F. Baletto and R. Ferrando, *Phys. Rev. Lett.*, 2004, **93**, 105503.
40 P. C. Kelires and J. Tersoff, *Phys. Rev. Lett.*, 1989, **63**, 1164–1167.

